Progress In Electromagnetics Research C, Vol. 105, 101–115, 2020

Surface Magnetic Resonance Tomography for Three-Dimensional Groundwater Using a Complex Model

Jian Chen, Yujing Yang, Ling Wan, and Tingting Lin*

Abstract—In recent years, surface magnetic resonance tomography (MRT), which is applied to the direct determination of the presence of groundwater, has been developed from underground two-dimensional to three-dimensional (3D) imaging. However, because of the influence of subsurface electrical conductivity, the magnetic resonance sounding (MRS) signal has been proved to be a complex-valued form. Moreover, the real and imaginary parts of MRS signals show different sensitivities to aquifers of different depths. In this study, a complex model of 3D MRT with separated loops configuration is introduced to provide accurate water-bearing imaging. Through simulation experiments, we demonstrate that the separated loops configuration is conducive to obtaining the imaginary part signal of MRS. Compared with a conventional model, the complex model has better 3D imaging resolution and sensitivity, especially for the deep regions. Moreover, in the case of noise interference and the presence of a multi-aquifer, the imaging results of complex inversion are reliable. As a result, this study is significant to the further development of multi-channel MRS instruments and provides a feasible method for high-precision imaging.

1. INTRODUCTION

Magnetic resonance sounding (MRS), which is also called magnetic resonance tomography (MRT) in two-dimensional (2D) or three-dimensional (3D) imaging, has gradually become one of the mainstream technologies used for groundwater exploration [1–3]. Among the known geophysical techniques, only MRS can supply direct quantitative information about the locations and amounts of free water in a subsurface [4]. With fresh water shortages becoming increasingly serious, there is an obvious motivation for developing MRT to explore underground aquifers. The core problem in MRS application is the limited detection depth. Because the MRS method uses single-frequency excitation, the penetration depth of the excitation field is typically within the top 100 m of the subsurface [30], and the imaging resolution decreases with increasing depth. Traditionally, initial amplitude inversion is used to quickly estimate the distribution of aquifers [5]. However, there is still much room for improvement in edge resolution, depth detection, and multi-aquifer recognition [6]. Thus, it is necessary to improve existing interpretation methods.

In previous publications on MRS technology, Legcheoko and Shushakov [7] first proposed the forward and inversion theory of initial amplitude interpretation method. They employed a coincident configuration to transmit an electromagnetic pulse for a given Larmor frequency, which generated an excitation magnetic field (EMF) that excited the hydrogen protons of a water molecule and collected the free induction decay (FID) signal whose amplitude reflects underground water-content distribution [2]. In early-epoch of research, the effective magnetic field was considered to be a perpendicular component of the EMF, which ignored the elliptic polarization and phase lag. Thus, the inversion results were undoubtedly influenced by modeling errors. To obviate this problem during theoretical modeling,

Received 19 June 2020, Accepted 28 August 2020, Scheduled 11 September 2020
* Corresponding author: Tingting Lin (ttlin@jlu.edu.cn).
The authors are with the College of Instrumentation and Electrical Engineering, Jilin University, Changchun 130026, China.

Weichman et al. [8] introduced the influence of electrical conductivity on MRS, which revealed that the MRS signal is complex-value with a definite phase, and both the real and imaginary parts of the signal are considered to contribute to the resolution of the inversion [9]. Braun et al. [10] proposed a complex inversion theory based on phase information and found that the imaginary part of the MRS kernel function was more sensitive to deep structures than the real part [11]. Later, Roy and lubczynski [6] demonstrated that detection and parameterization of a multi-aquifer would become possible when using both the amplitude and phase of the MRS signal. In terms of algorithm implementation, Müller-Petke et al. [12] pointed out that the key step of complex inversion is to separate the real and imaginary parts of complex data, producing a calculation program with complex Jacobian matrix. On this basis, Chen et al. [13] expanded the modelling to 2D with separated loops, which significantly decreased model ambiguities. Jiang et al. [14] continued to explore the stability and advantages of 2D QT complex inversion [15] and directly performed 3D QT inversion using complex data to improve imaging accuracy [16].

To date, the theoretical research of complex inversion mainly focuses on one-dimensional (1D) and 2D imaging, and its advantages and limitations in 3D applications have not yet been systematically verified. As the structure of natural groundwater often exists in non-layered form (e.g., groundwater under karst landform), 3D MRT technology for a complex model is analyzed in detail in this work. First, forward modeling and the complex inversion method for 3D MRT are reviewed and discussed. To evaluate the imaging results, the calculation formula of the 3D imaging resolution radius is derived. Then, through a series of simulation experiments, the layout of 3D high resolution detection loops is determined. By comparing it with the conventional initial amplitude inversion method, the advantages and limitations of the 3D complex inversion method are summarized and analyzed.

2. METHOD

2.1. Forward Modeling

Under the influence of a static geomagnetic field $\mathbf{B}_0$, the hydrogen protons in groundwater make spin precession around the $\mathbf{B}_0$ axis at a (angular) Larmor frequency $\omega_L = |\gamma \mathbf{B}_0|$. The gyromagnetic ratio for protons is $\gamma = 0.267518\,\mathrm{rad\ s^{-1}\ nT^{-1}}$. In MRS experiments, the hydrogen nucleus is excited from an equilibrium state to an excited state by alternating current (AC) at ω_L through a large transmitter loop (Tx) on the surface [4]. After the AC supply is turned off, the hydrogen nucleus gradually returns to an equilibrium state by releasing energy, which can be measured as an induced voltage (FID signal) in the receiver loop (Rx). Generally, the voltage response is given by [9, 17]:

$$\begin{aligned} E(q) \;=\; & -2\omega_L M_0 \int w(\mathbf{r}) \cdot \sin\left(-\gamma q \left|\mathbf{B}_{\mathrm{T}}^{+}(\mathbf{r},\rho(V))\right|\right) \cdot \left|\mathbf{B}_{\mathrm{R}}^{-}(\mathbf{r},\rho(V))\right| \cdot e^{i[\zeta_T(\mathbf{r},\rho(V))+\zeta_R(\mathbf{r},\rho(V))]} \\ & \times \left[\mathbf{b}_{\mathrm{R}}^{\perp}(\mathbf{r},\rho(V)) \cdot \mathbf{b}_{\mathrm{T}}^{\perp}(\mathbf{r},\rho(V)) + \mathrm{i}\mathbf{b}_0 \cdot \mathbf{b}_{\mathrm{R}}^{\perp}(\mathbf{r},\rho(V)) \times \mathbf{b}_{\mathrm{T}}^{\perp}(\mathbf{r},\rho(V))\right] d^3r \end{aligned} \tag{1}$$

where M_0 is the specific magnetization of the hydrogen nucleus; $w(\mathbf{r})$ is the free water content at location $\mathbf{r}$; q is the pulse moment; $\mathbf{B}_{\mathrm{T}}^{+}$ and $\mathbf{B}_{\mathrm{R}}^{-}$ are the co- and counter-rotating components of the excitation field, which depend on the resistivity ρ of the entire investigated volume V. $\mathbf{b}_0$ is the unit direction of the geomagnetic field; $\mathbf{b}_{\mathrm{R}}^{\perp}$ and $\mathbf{b}_{\mathrm{T}}^{\perp}$ are the unit direction of the transmitter field and virtual receiver field perpendicular to $\mathbf{b}_0$, respectively; and ζ_T and ζ_R are phase lags between the two loops and points $\mathbf{r}$ on the subsurface, which are also affected by resistivity. For the convenient representation of the MRS response, Equation (1) can be simplified to:

$$E(q) = \int K(q,\mathbf{r},\rho(V)) \cdot w(\mathbf{r}) d^3r \tag{2}$$

where $K(q,\mathbf{r},\rho(V))$ is the sensitivity kernel function; Equation (3) can be derived from Equations (1) and (2)

$$\begin{aligned} K(q,\mathbf{r},\rho(V)) \;=\; & 2\omega_L M_0 \sin\left(-\gamma q \left|\mathbf{B}_{\mathrm{T}}^{+}(\mathbf{r},\rho(V))\right|\right) \cdot \left|\mathbf{B}_{\mathrm{R}}^{-}(\mathbf{r},\rho(V))\right| \cdot e^{i[\zeta_T(\mathbf{r},\rho(V))+\zeta_R(\mathbf{r},\rho(V))]} \\ & \times \left[\mathbf{b}_{\mathrm{R}}^{\perp}(\mathbf{r},\rho(V)) \cdot \mathbf{b}_{\mathrm{T}}^{\perp}(\mathbf{r},\rho(V)) + \mathrm{i}\mathbf{b}_0 \cdot \mathbf{b}_{\mathrm{R}}^{\perp}(\mathbf{r},\rho(V)) \times \mathbf{b}_{\mathrm{T}}^{\perp}(\mathbf{r},\rho(V))\right] \end{aligned} \tag{3}$$

Equation (3) shows that $K(q, \mathbf{r}, \rho(V))$ is related to subsurface conductivity, pulse moment, loop size, and the characteristics of the geomagnetic field. Because it is affected by these complex factors, the kernel function is a complex-valued [11]. Equation (2) can be written in matrix notation as [3]:

$$\mathbf{E} = \mathbf{K}\mathbf{w} \tag{4}$$

After the kernel function is obtained, the solution for water content is converted to the inverse solution of Equation (4) because the observed data $\mathbf{E}$ are known. The commercial software COMSOL Multiphysics (Version 5.3) is utilized to subdivide the subsurface space for the accurate calculation of the magnetic field distribution. Moreover, the hammer integral algorithm [18, 19] based on an unstructured nonuniform tetrahedral mesh is applied to process the meshes; this limits the number of meshes, while ensuring computational accuracy. Notably, since MRS is an electromagnetic method, the excitation magnetic field depends on the resistivity of the subsurface, so resistivity is usually considered as a priori information or an inversion parameter, in the inversion process [29]. In most cases, priori information on geological conductivity is unknown. MRS method is usually combined with other electrical exploration methods (such as transient electromagnetic method) for joint data interpretation [32, 33]. Because this study focuses on the advantages and limitations of the 3D complex inversion method, the conductivity is treated as known a priori information, which has been proved to be feasible in relevant studies [13, 26, 29].

2.2. Model Resolution Calculation

Resolution is an effective parameter for analyzing the quality of MRT [20]. In order to evaluate imaging resolution accurately, the resolution radius of the forward model is introduced in this work. We use the sensitivity kernel singular value decomposition (SVD) method to determine the resolution matrix and resolution radius. The sensitivity kernel function $\mathbf{K}$ decomposed by SVD can be written as:

$$\mathbf{K} = \mathbf{U}\mathbf{S}\mathbf{V}^{\mathrm{T}} \tag{5}$$

where $\mathbf{U}$ is an orthogonal data matrix; $\mathbf{V}$ is an orthogonal eigenvector matrix; and $\mathbf{S}$ is a diagonal matrix. The resolution matrix of the model is defined as $\mathbf{R}_{\mathrm{m}}$, whose diagonal elements reflect the accuracy of the inversion results replacing the real results. The diagonal elements of $\mathbf{S}$ are defined as the filtering coefficient matrix $\mathbf{F}$, while the filtering coefficient f_i is given by [21]:

$$f_i = s_i^2 / \left(s_i^2 + \lambda^2\right) \tag{6}$$

$$\mathbf{R}_{\mathrm{m}} = \mathbf{V}\mathbf{F}\mathbf{V}^{\mathrm{T}} \tag{7}$$

where λ is the Tikhonov regularization parameter; s_i is a diagonal element of the diagonal matrix $\mathbf{S}$; and f_i represents the degree to which the Tikhonov regularization parameter affects the singular value matrix $\mathbf{S}$. Defining the resolution radius $\mathbf{R}_{\mathrm{d}}$ as the radius of a sphere, the equation is given by [22]:

$$\mathbf{R}_{\mathrm{d}} = \sqrt[3]{\mathbf{V}_{\mathrm{m}} / \left(\frac{4\pi}{3}\mathbf{R}_{\mathrm{m}}\right)} \tag{8}$$

As mentioned above, finite-element software is used to divide the 3D subsurface space into volume elements. The volume matrix $\mathbf{V}_{\mathrm{m}}$ is in the matrix form of the volume of all the subsurface subdivision elements. The resolution radius $\mathbf{R}_{\mathrm{d}}$ intuitively reflects the size of the diagonal elements of $\mathbf{R}_{\mathrm{m}}$, which can be used to estimate the imaging resolution. The smaller the resolution radius is, the higher the resolution is.

2.3. Complex Inversion Method

Because of elliptical polarization and other factors, the observed MRS data $\mathbf{E}$ and kernel function $\mathbf{K}$ are both complex-valued. Representing the real part of the kernel function with $\mathbf{A}$ and the imaginary part with $\mathbf{B}$, Equation (4) can be written as:

$$\mathrm{real}(\mathbf{K}) = \mathbf{A} \tag{9}$$

$$\mathrm{imag}(\mathbf{K}) = \mathbf{B} \tag{10}$$

$$|\mathbf{E}| = |\mathbf{K}\mathbf{w}| = \sqrt{(\mathbf{A}\mathbf{w})^2 + (\mathbf{B}\mathbf{w})^2} \tag{11}$$

In a conventional model, a Jacobian transformation is used, and the complex kernel is converted into a real value by taking the moduli of both sides of the equation; this results in a loss of the phase information. In the complex model, assuming that the phase offset of all pulse moments and time is constant, the following formulas can be obtained by processing the imaginary parts and the real part of the MRS signal expression separately:

$$\mathbf{E}_{\text{comp}} = \mathbf{K}_{\text{comp}} \cdot \mathbf{w} \tag{12}$$

$$\text{real}(\mathbf{E}) = \text{real}(\mathbf{K}\mathbf{w}) = \mathbf{A}\mathbf{w} \tag{13}$$

$$\text{imag}(\mathbf{E}) = \text{imag}(\mathbf{K}\mathbf{w}) = \mathbf{B}\mathbf{w} \tag{14}$$

By extracting the real part and imaginary part data of the MRS signal and kernel function, a new data array for inversion is constructed [12], which can be inverted without losing phase information. It should be pointed out that non-resonant excitation and hardware-related phenomena (i.e., resonant tuning of receiver loops) also affect signal phase [4, 14, 23], but they are ignored here.

To obtain the water-content distribution, we employed the Tikhonov regularization [24] solution. The optimization problem of the objective function Φ was solved by adding a smoothing constraint condition. The resulting optimization problem is given by:

$$\Phi = \|\mathbf{D}\left(\mathbf{E}_{\text{comp}} - \mathbf{K}_{\text{comp}} \cdot \mathbf{w}\right)\|_2^2 + \lambda\|\mathbf{C} \cdot \mathbf{w}\|_2^2 \rightarrow \min \tag{15}$$

where $\mathbf{D}$ is the error estimate for the observed data, which satisfies $\mathbf{D} = 1/\boldsymbol{\varepsilon}_d$; $\boldsymbol{\varepsilon}_d$ is the covariance matrix of observation data and fitting data. $\mathbf{E}_{\text{comp}}$ and $\mathbf{K}_{\text{comp}}$ are the new matrices obtained by separating the real and imaginary parts of the data sets $[\mathbf{E}_{\text{real}}, \mathbf{E}_{\text{imag}}]^{\text{T}}$ and $[\mathbf{K}_{\text{real}}, \mathbf{K}_{\text{imag}}]^{\text{T}}$; λ is the weighting factor that balances the data-fit error and smoothness of the model [21]. The smoothness matrix $\mathbf{C}$, as a derivate operator, defines the order of the Tikhonov solution and the degree of smoothness, which ensures that stable smoothness constraints can be obtained in all meshes [31]. The function in Equation (15) can be minimized by iteratively updating the water-content model

$$\mathbf{w}^{\ell+1} = \mathbf{w}^{\ell} + \eta^{\ell}\Delta\mathbf{w}^{\ell} \tag{16}$$

where ℓ is the iteration number, and η^{ℓ} is the line-search parameter. The updated value $\Delta\mathbf{w}^{\ell}$ of the model can be calculated by solving the following Gauss-Newton system of equations [4, 25]

$$\left(\mathbf{K}_{\text{comp}}^{\text{T}}\,\mathbf{D}^{\text{T}}\mathbf{D}\mathbf{K}_{\text{comp}} + \lambda\mathbf{C}^{\text{T}}\mathbf{C}\right)\Delta\mathbf{w}^{\ell} = \mathbf{K}_{\text{comp}}^{\text{T}}\,\mathbf{D}^{\text{T}}\mathbf{D}\left(\mathbf{E}_{\text{comp}} - \mathbf{K}_{\text{comp}} \cdot \mathbf{w}^{\ell}\right) - \lambda\mathbf{C}^{\text{T}}\mathbf{C}\mathbf{w}^{\ell} \tag{17}$$

where T is the matrix transpose.

3. SYNTHETIC RESULTS

3.1. High Resolution 3D Detection Loops Layout

The layout of the detection loops affects the quality of imaging. In recent years, the view that a separated-loop configuration can improve lateral imaging resolution has been widely recognized and tested [19, 26]. To evaluate the influence of loop-layout on a 3D complex model, the configurations of the separated-loop and coincident-loop, as shown in Fig. 1, are provided for comparison.

For the convenience of distinguishing the detection loops, a coordinate system is used to mark the position of the loops in abscissa and ordinate coordinates, and a coordinate system from -75 m to 75 m is evenly marked as 0 to 6, with an interval of 25 m. In the coincident case, there are 13 transmitters (Tx13, Tx22, Tx23, Tx24, Tx31, Tx32, Tx33, Tx34, Tx35, Tx42, Tx43, Tx44, and Tx53), and each transmitter loop corresponds to an overlapping receiver loop [27]. In the separated case, there are only nine transmitters (without Tx23, Tx32, Tx34, and Tx43); since the model is based on a four-channel instrument, each measurement group contains one transmitter loop and four receiver loops (including an overlapping loop); for example, the receiver loops for Tx13 are Rx03, Rx12, Rx13, and Rx14. All transmitter and receiver loops are single-turn square coils of 50 m $\times$ 50 m. The detection depth of the MRS instrument is positively correlated with the size of the transmitter and receiver [14]. Generally, the effective detection depth for a square coincident-loop with side length 50 m is 50 m. In this work, we focus on an MRS imaging resolution of 50 m. Additionally, we compare the resolution and imaging results for the above cases from 10 m to 50 m underground.

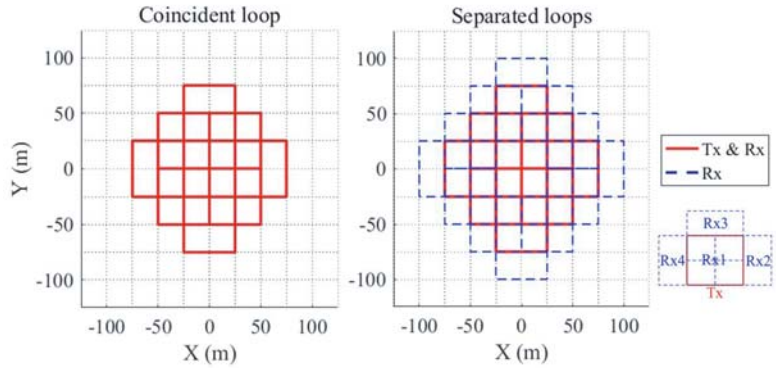

Figure 1. Arrangement models of Coincident loop and Separated loops.

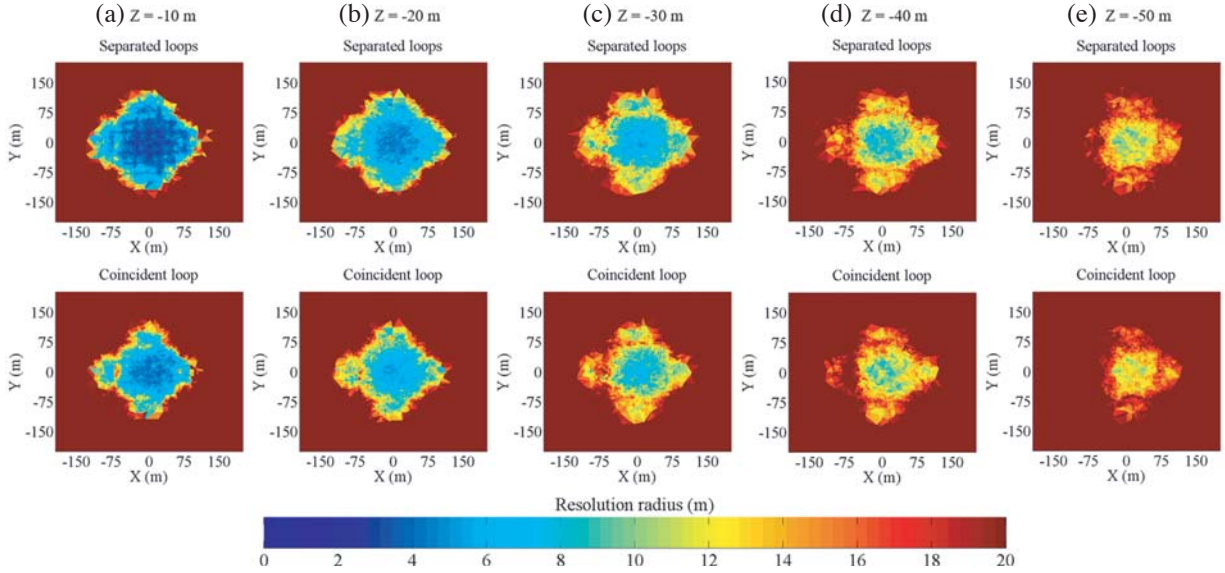

Figure 2. Resolution radii of two configurations. The first row and the second row represent the resolutions of the separated loops and the coincident loop, respectively; Z represents the subsurface depth.

Figure 2 shows that the optimum resolution positions of both configurations are concentrated in the vicinity of the transmitter loop. The configuration of separated loops has a smaller resolution radius than that of the coincident loop, which means that the separated loops have a higher resolution. At an interface of 10 m directly below the transmitter loops, the resolution radius of the separation-loop can reach about 1 m, while that of the coincident-loop can only reach 2 m. Resolution decreases with depth, and ultimately the resolution radius of the two configurations at 50 m subsurface is about 10 m. Under the influence of a geomagnetic field, the resolution in the East-West (along the X-axis) direction is asymmetric, and this asymmetry is evident with increasing detection depth. On this basis, an inversion experiment is designed to compare the image quality of the two configurations.

We construct two identical aquifers symmetrically along the XZ plane, whose lengths, widths, and heights are 30 m, 30 m, and 15 m, respectively. Fig. 3(a) shows two aquifers located at 10–25 m underground with a central spacing of 10 m. It should be pointed out that the burrs on the edge of the aquifer model can be improved by increasing the precision of the edge meshing. The water-content distribution is presented in three sections of XY ($Z = 0$ m) plane, YZ ($X = 0$ m) plane, and XZ ($Y = 0$ m) plane. The geomagnetic field is 54752 nT; the absolute temperature is 293 K; the water

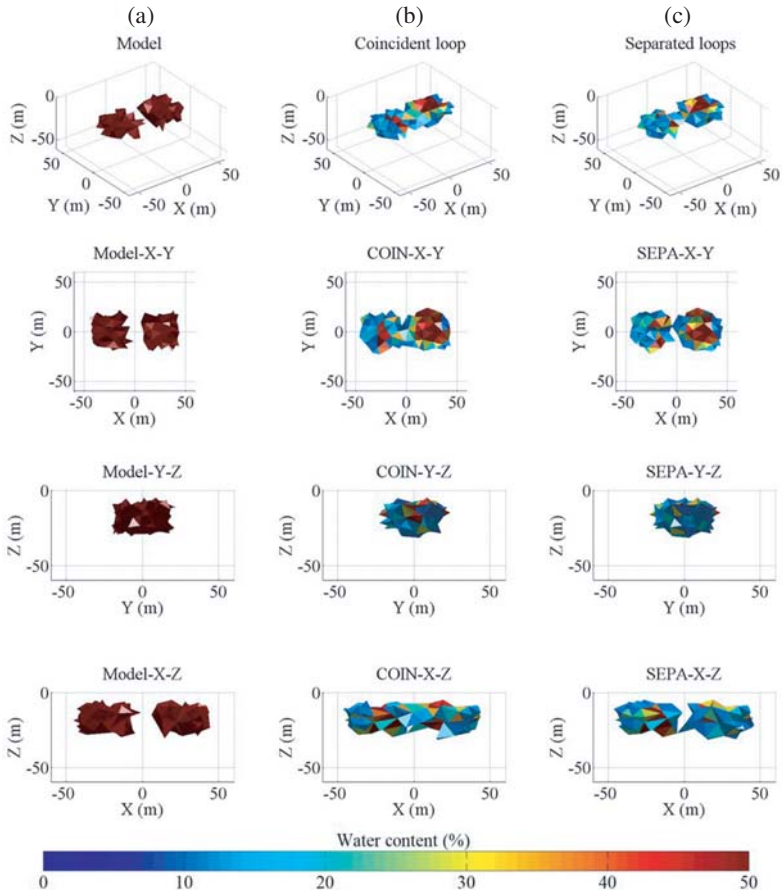

Figure 3. Inversion results of two configurations ((a) aquifer model, (b) coincident loop, (c) separated loops; both aquifers are set at 10–25 m underground; the minimum distance between the two aquifers is 10 m). The water-content distribution is presented in three sections of the XY ($Z = 0$ m) plane, YZ ($X = 0$ m) plane, and XZ ($Y = 0$ m) plane; the scheme of initial amplitude inversion is employed to interpret the data.

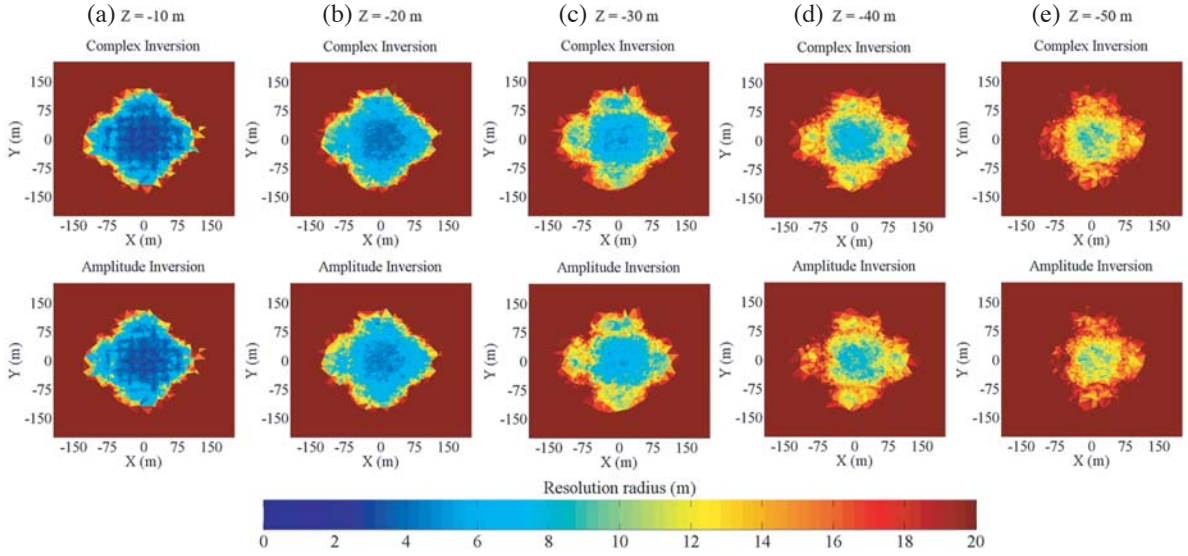

Figure 4. Resolution radii of the two inversion methods. The first row and the second row represent the resolutions of complex inversion and amplitude inversion, respectively; Z represents the subsurface depth.

content of the aquifer is 50%; the half-space resistivity is set to $1000\,\Omega \cdot \mathrm{m}$; the number of transmitting pulse moments is set to 40, varying from $0.1\mathrm{A} \cdot \mathrm{s}$ to $10\ \mathrm{A} \cdot \mathrm{s}$ logarithmically; Tx and Rx have one turn; and 5 nV Gaussian noise is added to the synthetic MRS data. After the model was built, we employed the scheme of initial amplitude inversion to interpret the data. From an analysis of the resolution radius (Fig. 2), it can be seen that when the depth of the aquifer is 20 m, the lateral effective resolution radius of the separated loops configuration is $6 \sim 8$ m, while the coincident loop is about 10 m, which indicates that the coincident loop may not be able to distinguish the two aquifers.

The MRT results of the two configurations are shown in Fig. 3(b), which shows that both configurations locate the aquifer roughly. The imaging results of the coincident loop cannot effectively distinguish between the two aquifers and have low edge resolution, while the separated loops can distinguish between the two aquifers with a better imaging resolution. The imaging results are consistent with the resolution radius results discussed earlier. Accordingly, the separated loops configuration is used to improve 3D imaging quality in the remainder of this work.

3.2. Inversion Results

Relevant research indicates that complex inversion can provide better results than amplitude inversion [6, 11]. To confirm this, we compared the imaging quality of the complex inversion with that of the conventional amplitude inversion for a 3D water-bearing structure. Firstly, as shown in

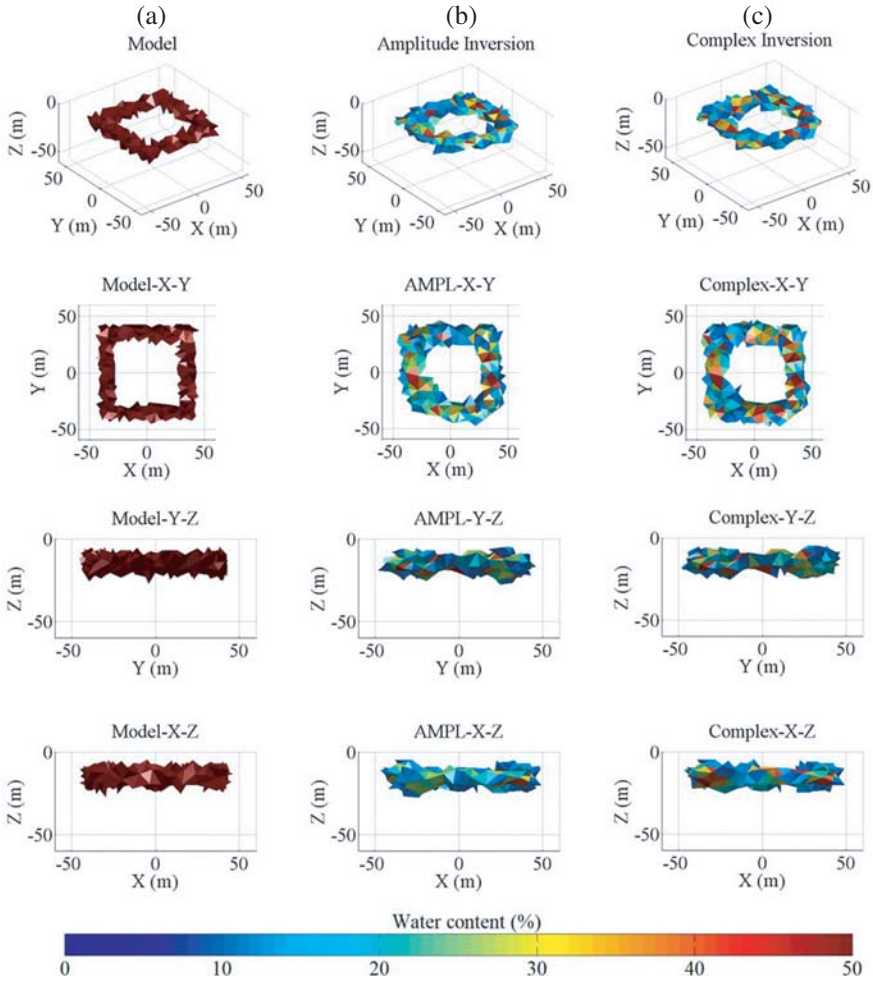

Figure 5. Imaging results of amplitude inversion and complex inversion ((a) aquifer model, (b) amplitude inversion, (c) complex inversion; the aquifer is set at 10–20 m depth).

Fig. 4, the resolution radius of the two inversion schemes is calculated. In a range of about 20 m from the subsurface, the resolution radii of the two schemes are almost the same. When depth exceeds 20 m, the resolution radius of the complex model is relatively small, which means that resolution is relatively high; this trend becomes more obvious with increasing depth.

In addition, we established a hollow square water body model, as shown in Fig. 5(a), which is set at 10–20 m depth. This model is mainly located in the boundary region, which allows a good comparison between the differences in resolution of two methods. The outer length of the square aquifer is 80 m; the inner length is 60 m; and the height is 10 m. The geomagnetic field is 54752 nT; the absolute temperature is 293 K; the water content of the aquifer is 50%; the half-space resistivity is set to $1000\,\Omega \cdot \mathrm{m}$; the number of transmitting pulse moments is set to 40, varying from $0.1\mathrm{A} \cdot \mathrm{s}$ to $10\,\mathrm{A} \cdot \mathrm{s}$ logarithmically; Tx and Rx have one turn; and 5 nV Gaussian noise is added to the synthetic MRS data.

The imaging results of the two inversion schemes are illustrated in Fig. 5. Both inversion schemes can image the aquifer model, and the imaging results reflect the characteristics of the model. The results indicate that the two schemes have similar resolutions in shallow aquifers, which is consistent with the results of resolution radius discussed earlier. On this basis, we continued to increase the depth of the model and set the aquifer at 20–30 m underground, while other conditions remained unchanged. Fig. 6 shows that amplitude inversion can barely image the aquifer in this case, while the complex inversion scheme still maintains good imaging quality. This indicates that complex inversion has obvious advantages in depth detection.

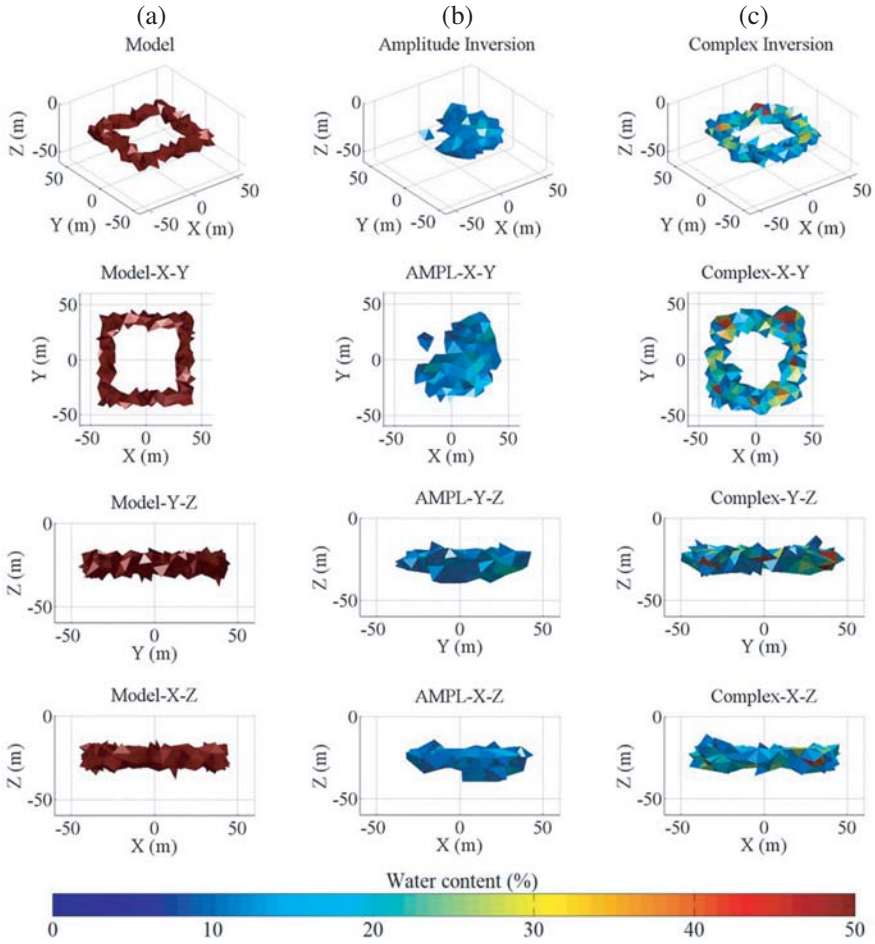

Figure 6. Imaging results of amplitude inversion and complex inversion ((a) aquifer model, (b) coincident loop, (c) separated loops; the aquifer is set at 20–30 m depth).

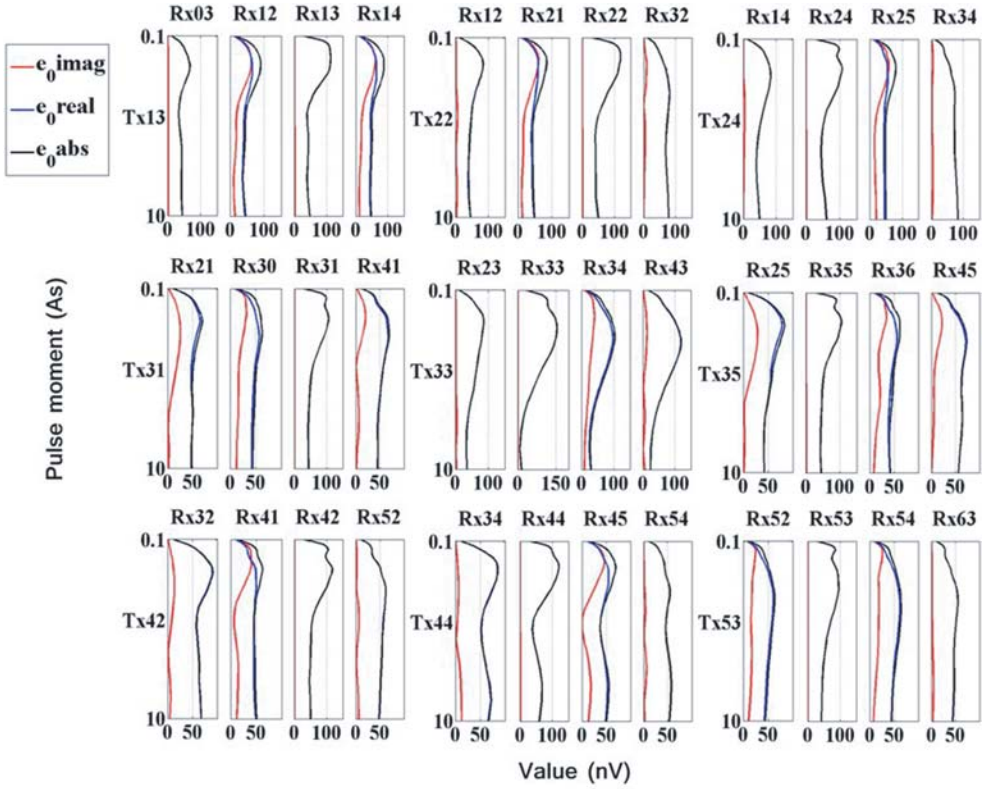

Figure 7. Sounding curves of the aquifer model measured by separated loops (the aquifer model is shown in Fig.? 6(a); the signal amplitude is represented by the black line, the real part of the signal is represented by the blue line, and the imaginary part of the signal is represented by the red line).

3.3. Sounding Curves

To further analyze the relationship between the real and imaginary parts and the amplitude of the MRS signal, this work calculates the sounding curves of the aquifer model (Fig. 6(a)) measured by separated loops. The results of pulse moments response for real and imaginary parts are shown in Fig. 7. The imaginary part of the MRS signal exists only when the receiver loops and transmitter loops do not overlap. The reason for this can be traced to Equation (3). The second line of Equation (3) accounts for the geometric relationships of the loop fields. It is unity for a coincident loop configuration (i.e., $\mathbf{b}_{\mathrm{R}}^{\perp} = \mathbf{b}_{\mathrm{T}}^{\perp}$), but has complex values in the range $[-1, 1]$ $[-i; i]$ for a separated loop configuration, which will reduce the signal amplitudes and cause geometry related phase lags [4]. Further observation shows that the signals of the receiver loops on both sides of the transmitter in the north and south directions show an approximate symmetry trend, while the signals in the east and west directions are asymmetric due to the influence of the geomagnetic field. In conclusion, both the real and imaginary parts of the MRS signal constitute the received signal. When considering the amplitude of the signal only, the phase information of the signal is lost, resulting in a decline in imaging accuracy. Thus, the separated loops configuration is conducive to obtaining a complex signal of MRS.

4. DISCUSSION

4.1. Noise Effect

Noise is always unavoidable in field experiments. Therefore, studying the inversion results of a complex model with noise interference is necessary. In this work, we discuss the imaging quality of complex inversion when Gaussian random noise at levels of 0 nV, 1 nV, 5 nV, and 10 nV is added to the MRS

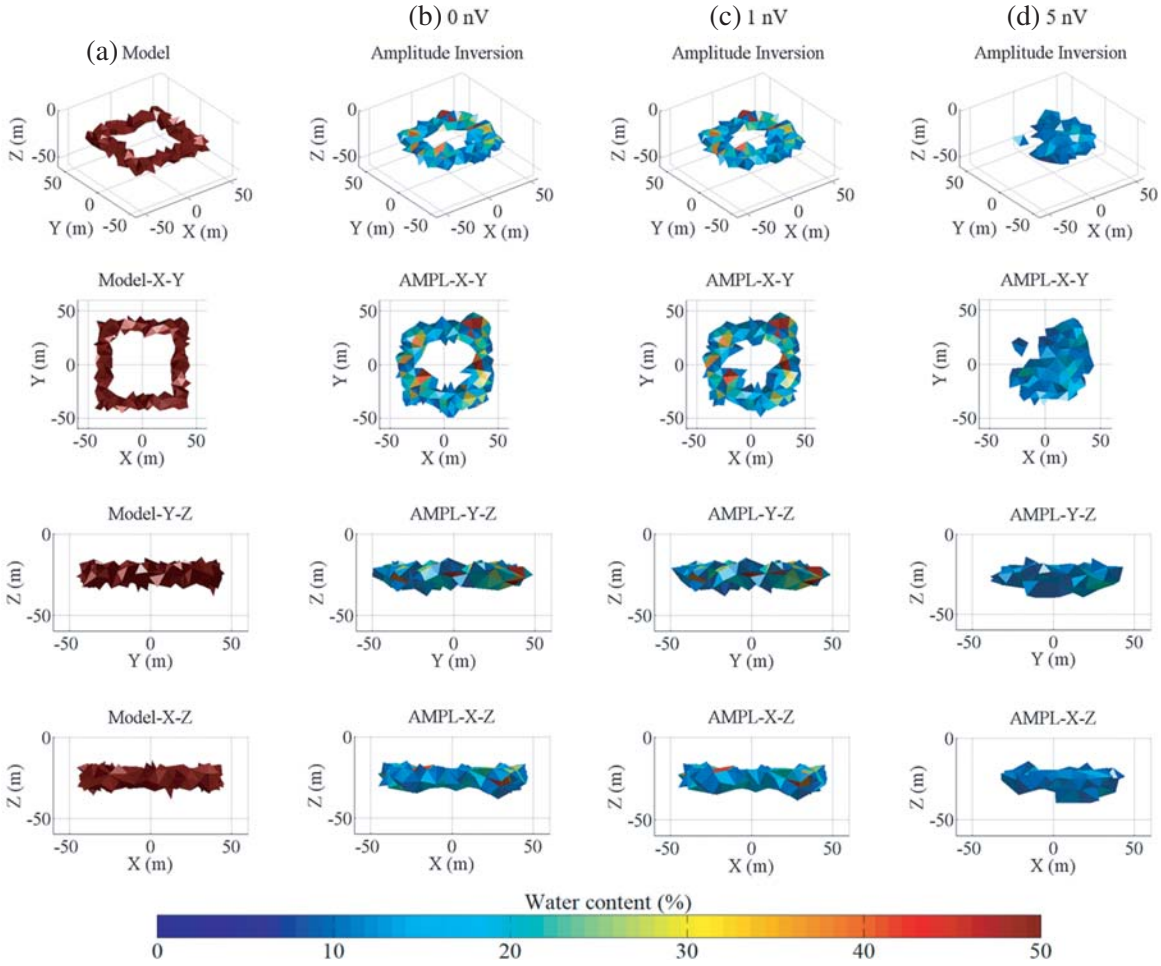

Figure 8. Imaging results of amplitude inversion. (a) The aquifer model is set at 20–30 m subsurface, with (b) 0 nV, (c) 1 nV, and (d) 5 nV Gaussian random noise added to the MRS data.

data, and compare the imaging results of the same conditions with the conventional amplitude inversion. The 3D aquifer model is shown in Fig. 8(a), and the model parameters are the same as those in Fig. 6(a). The amplitude of the MRS signal is about 100 nV, which means that the noise level is about 0%, 1%, 5%, and 10% of the MRS signal. Conventional amplitude inversion imaging results are shown in Fig. 8, while complex inversion results are shown in Fig. 9. The two schemes are not affected much with a noise of 1 nV (about 1% of the MRS signal), except for slight variations in the water-content distribution and an increase in boundary burrs. When the level of noise reaches 5 nV (about 5% of the MRS signal), the imaging quality of the amplitude inversion worsens, while that of the complex inversion is relatively stable. That is to say, complex inversion has higher anti-noise capability than amplitude inversion. However, the complex model is also sensitive to noise, and the imaging quality becomes poor when the noise reaches 10 nV (about 10% of the MRS signal).

4.2. Two Aquifers Effect

Complex inversion has advantages in deep detection, and whether it has good imaging capabilities in complex 3D water-bearing structures is worth further discussion. Therefore, we analyzed the imaging quality of the complex model for two underground aquifers. We still used the hollow-square aquifer model mentioned above. The two aquifers are set at 0–10 m and 20–30 m underground, and the minimum distance between the two is only 10 m. The number of transmitting pulse moments is set to 40, varying

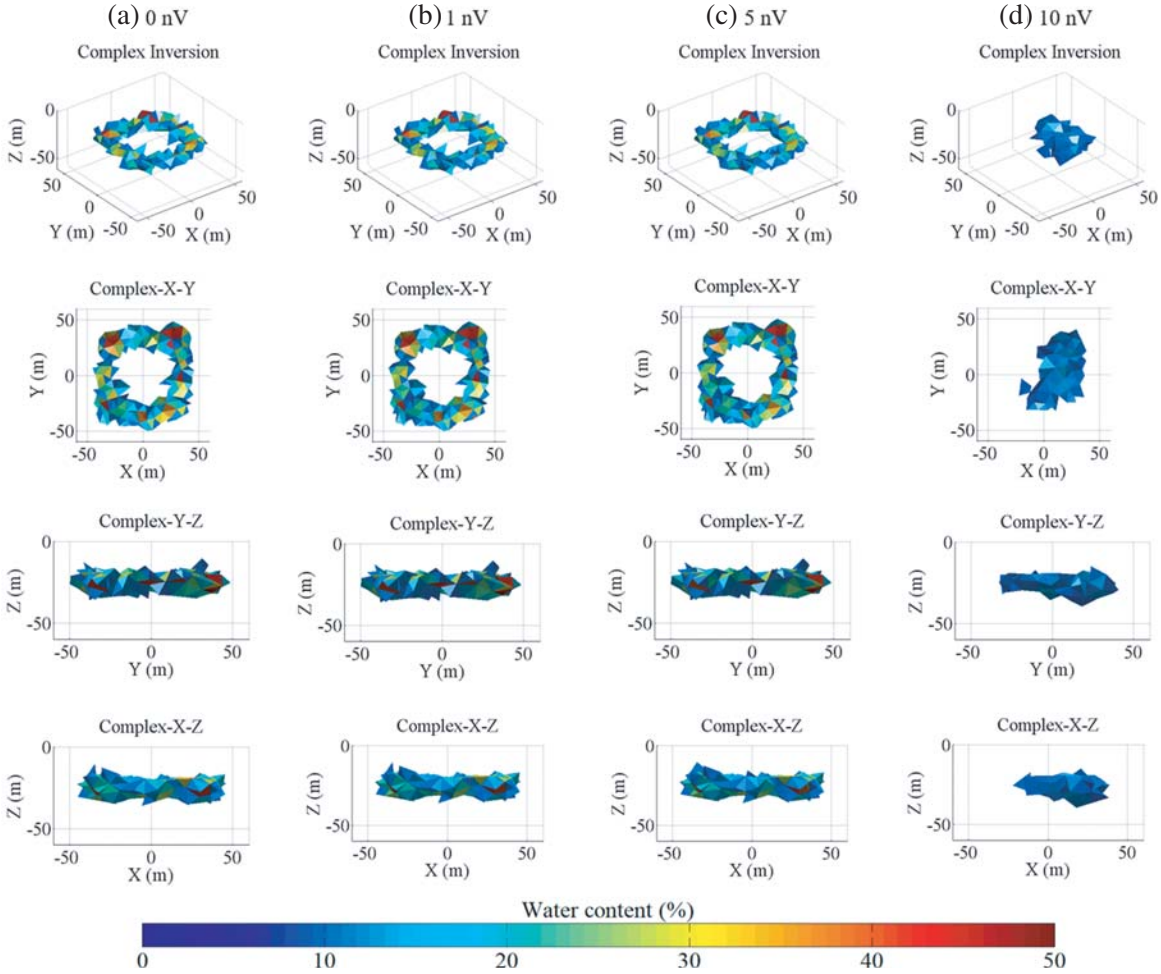

Figure 9. Imaging results of complex inversion. The aquifer model is the same as that in Fig. 8(a), with (a) 0 nV, (b) 1 nV, (c) 5 nV, and (d) 10 nV Gaussian random noise added to the MRS data.

from 0.1 A · s to 10 A · s logarithmically, and 0 nV and 5 nV Gaussian noises are added to the MRS data. The imaging results are shown in Fig. 10. When 0 nV noise is added, the complex inversion scheme can effectively distinguish between the two aquifers. The imaging results worsen when 5 nV Gaussian noise is added, but the positions and rough outlines of the two aquifers can be visualized. The overall imaging results are basically consistent with the constructed model, which indicates that complex inversion improves the imaging quality of complex water-bearing structures.

4.3. Conductivity Effect

Section 2.1 mentions that the MRS signal is affected by subsurface conductivity, and the MRS signal is mainly determined by its kernel function. The change in relative proportion of the real and imaginary parts of the kernel function reflects the change in phase. To study the effect of conductivity on the MRS signal, slice diagrams are presented of the kernel function for homogeneous half-space with resistivities between 1 and 1000 Ω · m (Fig. 11). Due to electromagnetic attenuation, the value of the kernel function decreases with decreasing resistivity, but the proportion of the imaginary part of the kernel function increases gradually. When the resistance value is more than 100 Ω · m, the MRS kernel function is mainly determined using its real component, and the amplitude and phase change gradually become stable. Our results agree with those of Braun and Yaramanci [29]. Thus, a priori information regarding subsurface conductivity is needed for more accurate data interpretation.

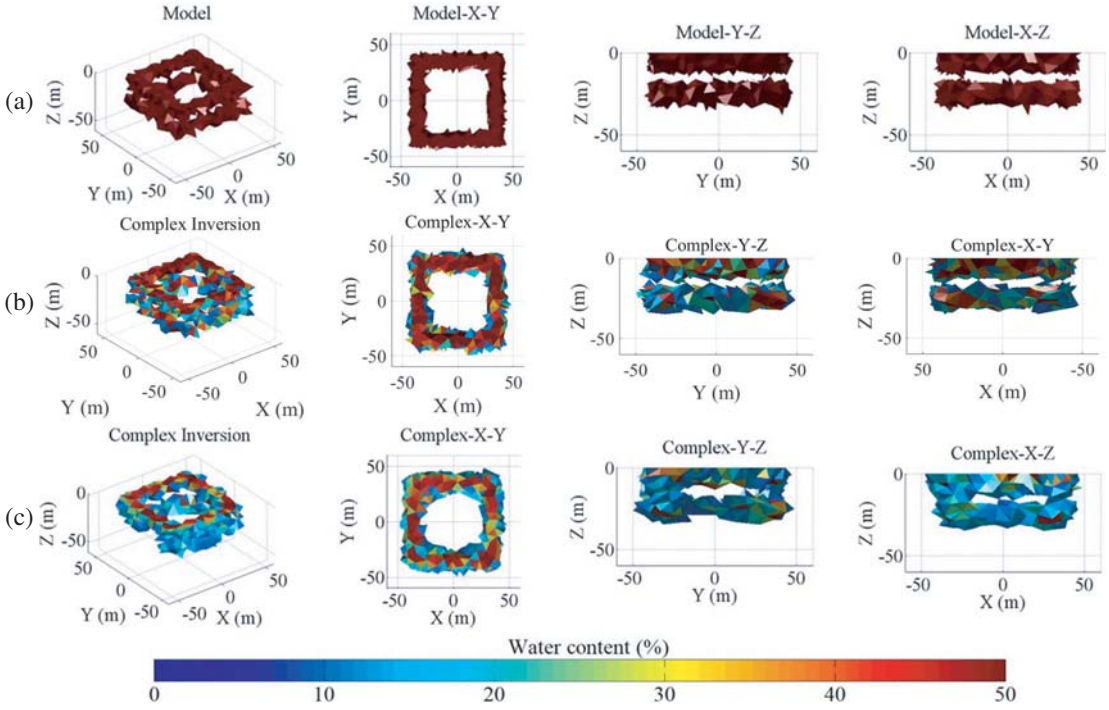

Figure 10. Imaging results of complex inversion for two aquifers. The first aquifer is set at 0–10 m underground and the second aquifer is set at 20–30 m subsurface: (a) aquifer model, complex inversion with (b) 0 nV, (c) 5 nV Gaussian random noise added to the MRS data.

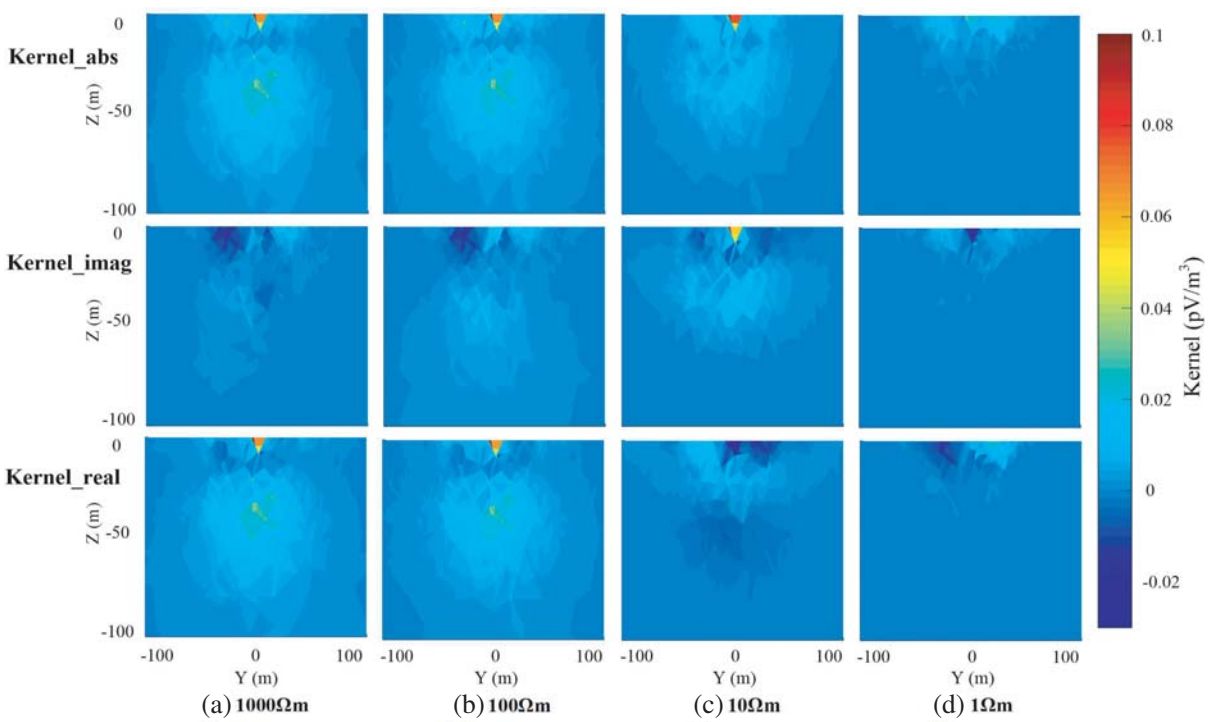

Figure 11. Slice diagram of the kernel functions for a homogeneous half-space with resistivities between 1 and 1000 $\Omega \cdot$ m. From the first row to the third row, the absolute value, and the imaginary and real parts of the kernel function are shown (YZ ($X = 0$ m) plane).

5. CONCLUSION

Research in high-precision MRT technology is of critical significance to groundwater detection. Conventional models use the amplitude of the MRS signal to locate aquifers and ignore phase information. By separating the real and imaginary parts of MRS data, a 3D complex model of MRS inversion provides an accurate imaging result for water-bearing structures. Using two comparative experiments, we prove that the separated loops configuration is conducive to extracting a complex MRS signal, and that complex inversion has a higher depth resolution than amplitude inversion. The simulation results agree well with the calculated resolution radius. Complex model imaging quality for noisy interference and multi-aquifer cases is discussed. When the noise level is lower than 10% of the MRS signal, the imaging results of complex inversion are relatively stable and reliable. However, the implementation of the algorithm needs further improvement of the instrument, because it is difficult to acquire complex-value MRS data using existing instruments. In addition, existing multi-channel instruments can only support eight to twelve channels of acquisition [28], which is not sufficient for high-efficiency 3D detection. Thus, further development of instruments with more acquisition and transmission channels is expected to improve the practicability of the complex inversion algorithm.

ACKNOWLEDGMENT

This research was supported by the National Science Fund for Excellent Young Scholars (41722405), the National Natural Science Foundation of China (41874209), the Key Research Projects of Jilin Provincial Science and Technology Department (20180201017GX) and International Cooperation Project of Science and Technology Department of Jilin Province (20200801007GH).

REFERENCES

1. Yaramanci, U., "Surface Nuclear Magnetic Resonance (SNMR) — A new method for exploration of ground water and aquifer properties," *Annali di Geofisica*, Vol. 43, No. 6, 1159–1175, 2000.
2. Lubczynski, M. and J. Roy, "Magnetic resonance sounding: New method for ground water assessment," *Groundwater*, Vol. 42, No. 2, 291–309, 2004.
3. Hertrich, M., M. Braun, T. Gunther, A. G. Green, and U. Yaramanci, "Surface nuclear magnetic resonance tomography," *IEEE Transactions on Geoscience and Remote Sensing*, Vol. 45, No. 11, 3752–3759, 2007.
4. Hertrich, M., A. G. Green, M. Braun, and U. Yaramanci, "High-resolution surface-NMR tomography of shallow aquifers based on multi-offset measurements," *Geophysics*, Vol. 74, No. 6, 47–59, 2009.
5. Braun, M. and U. Yaramanci, "Resistivity inversion of magnetic resonance sounding — Assessment of sensitivity and reliability," *Near Surface 2007 — 13th EAGE European Meeting of Environmental and Engineering Geophysics Conference*, 2007, DOI: 10.3997/2214-4609.20146609.
6. Roy, J. and M. W. Lubczynski, "Exploiting the MRS-phase information to enhance detection of masked deep aquifers: Examples from the Netherlands," *Near Surface Geophysics*, Vol. 12, No. 2, 309–324, 2014.
7. Legchenko, A. V. and O. A. Shushakov, "Inversion of surface NMR data," *Geophysics*, Vol. 63, No. 1, 75–84, 1998.
8. Weichman, P. B., E. M. Lavely, and M. Ritzwoller, "Surface nuclear magnetic resonance imaging of large systems," *Physical Review Letters*, Vol. 82, No. 20, 4102–4105, 1999.
9. Weichman, P. B., E. M. Lavely, and M. H. Ritzwoller, "Theory of surface nuclear magnetic resonance with applications to geophysical imaging problems," *Physical Review Letters*, Vol. 62, No. 1, 1290–1312, 2000.
10. Braun, M., M. Hertrich, and U. Yaramanci, "Complex inversion of surface-NMR signals — Extending the limits of model resolution," *Symposium on the Application of Geophysics to Engineering and Environmental Problems Conference*, No. 0, 856–867, 2004.

11. Braun, M., M. Hertrich, and U. Yaramanci, "Study on complex inversion of magnetic resonance sounding signals," *Near Surface Geophysics*, Vol. 3, No. 3, 155–163, 2005.
12. Müller-Petke, M., M. Braun, M. Hertrich, S. Costabel, and J. Walbrecker, "MRSmatlab — A software tool for processing, modeling, and inversion of magnetic resonance sounding data," *Geophysics*, Vol. 81, No. 4, 9–21, 2016.
13. Chen, B., X. Hu, J. Li, and Y. Liu, "Complex inversion of MRT signals under different loop configurations for groundwater exploration," *Groundwater*, Vol. 55, No. 2, 171–182, 2017.
14. Jiang, C. D., M. Müller-Petke, Q. Wang, and J. Igel, "Two-dimensional QT inversion of complex magnetic resonance tomography data," *Geophysics*, Vol. 83, No. 6, 65–75, 2018.
15. Müller-Petke, M. and U. Yaramanci, "QT inversion — Comprehensive use of the complete surface NMR data set," *Geophysics*, Vol. 75, No. 4, 199–209, 2010.
16. Jiang, C. D., G. Du, and T. Lin, "Magnetic resonance tomography for 3-D water-bearing structures using a loop array layout," *IEEE Transactions on Geoscience and Remote Sensing*, Vol. 57, No. 7, 4544–4557, 2019.
17. Hertrich, M., M. Braun, and U. Yaramanci, "Magnetic resonance soundings with separated transmitter and receiver loops," *Near Surface Geophysics*, Vol. 3, No. 3, 141–154, 2005.
18. Yu, J., "Symmetric gaussian quadrature formulae for tetrahedronal regions," *Computer Methods in Applied Mechanics and Engineering*, Vol. 43, No. 3, 349–353, 1984.
19. Jiang, C. D., M. Müller-Petke, J. Lin, and U. Yaramanci, "Imaging shallow three-dimensional water-bearing structures using magnetic resonance tomography," *Journal of Applied Geophysics*, Vol. 116, No. 0, 17–27, 2015.
20. Friedel, S., "Resolution, stability and efficiency of resistivity tomography estimated from a generalized inverse approach," *Geophysical Journal of the Royal Astronomical Society*, Vol. 153, No. 2, 305–316, 2003.
21. Müller-Petke, M. and U. Yaramanci, "Resolution studies for Magnetic Resonance Sounding (MRS) using the singular value decomposition," *Journal of Applied Geophysics*, Vol. 66, Nos. 3–4, 165–175, 2008.
22. Günther, T., "Inversion methods and resolution analysis for the 2D/3D reconstruction of resistivity structures from DC measurements," *University of Mining and Technology Freiberg*, 2004.
23. Levitt, M. H., "The signs of frequencies and phases in NMR," *Journal of Magnetic Resonance*, Vol. 126, No. 1, 164–182, 1997.
24. Tikhonov, A. N. and V. Y. Arsenin, *Solutions of Ill-Posed Problems*, V. H. Winston and Sons, Washington DC, 1997.
25. Günther, T., C. Rücker, and K. Spitzer, "Three-dimensional modelling and inversion of dc resistivity data incorporating topography — II. Inversion," *Geophysical Journal of the Royal Astronomical Society*, Vol. 166, No. 2, 506–517, 2006.
26. Jiang, C. D., M. Müller-Petke, J. Lin, and U. Yaramanci, "Magnetic resonance tomography using elongated transmitter and in-loop receiver arrays for time-efficient 2-D imaging of subsurface aquifer structures," *Geophysical Journal International*, Vol. 200, No. 2, 824–836, 2015.
27. Legchenko, A., M. Descloitres, C. Vincent, H. Guyard, H. Garambois, K. Chalikakis, and M. Ezersky, "Three-dimensional magnetic resonance imaging for groundwater," *New Journal of Physics*, Vol. 13, No. 2, 1367–2630, 2011.
28. Lin, T., M. Chen, W. Du, and J. Zhao, "Signal acquisition module design for multi-channel surface magnetic resonance sounding system," *Review of Scientific Instruments*, Vol. 86, No. 11, 0034–6748, 2015.
29. Braun, M. and U. Yaramanci, "Inversion of resistivity in Magnetic Resonance Sounding," *Journal of Applied Geophysics*, Vol. 66, Nos. 3–4, 151–164, 2008.
30. Behroozmand, A. A., K. Keating, and E. Auken, "A review of the principles and applications of the NMR technique for near-surface characterization," *Surveys in Geophysics*, Vol. 36, No. 1, 27–85, 2015.

31. Yaramanci, U. and M. Müller-Petke, "Improvements in inversion of magnetic resonance exploration water content, decay time, and resistivity," *Journal of Earth Science*, Vol. 20, No. 3, 592–605, 2009.
32. Behroozmand, A. A., E. Auken, G. Fiandaca, and A. Christiansen, "Improvement in MRS parameter estimation by joint and laterally constrained inversion of MRS and TEM data," *Geophysics*, WB191–WB200, 2012.
33. Vilhelmsen, T. N., A. A. Behroozmand, S. Christensen, and T. H. Nielsen, "Joint inversion of aquifer test, MRS, and TEM data," *Water Resources Research*, Vol. 50, No. 4, 3965–3975, 2014.